**SIRM 2019 – 13th International Conference on Dynamics of Rotating Machines,
Copenhagen, Denmark, 13th – 15th February 2019**

Numerical Description of a Rotor Supported by Gas Polymer Bearings for Time Domain Simulations - Implementation and Parametrization of the Structure Model

Gregor Schilling [1], **Katja Bäuerlein** [1], **Robert Liebich** [1]

[1] Engineering Design and Product Reliability, Technical University Berlin, 10623, Berlin, Germany, gregor.schilling@tu-berlin.de

Abstract

Gas Polymer Bearings (GPBs) have a wide range of usability as replacements for common Gas Foil Journal Bearings (GFBs). The most important benefit of these kind of bearings is the simple manufacturing process and the wide range of suitable materials for many applications for example in organic rankine cycle processes and turbomachinery in food industry. The present work examines the implementation of a viscoelastic model of the structure to describe the behavior of polymer materials and their frequency dependent stiffness and damping characteristic. The model is based on discrete rheological elements and embedded into a transient model of a rotor bearing system (RBS). Following the model description, the parametrization process of the rheological elements is explained. Finally the results of transient simulations of a rotor-bearing-system are presented and discussed with regards to the parametrization process.

1 Introduction

In the field of rotating machinery at high speeds hydrodynamic air bearings have many advantages in comparison to common rolling bearings or oil based hydrostatic and hydrodynamic bearings. The most important benefits are the simple bearing system design without additional lubrication components, the low abrasive wear and the high degree of efficiency in case of the small friction torque. Due to the low viscosity of gases, air bearings exhibit a lower load capacity and damping ratio in comparison to oil lubricated bearings. Another problem is the occurrence of nonlinear sub- and super harmonic vibrations, which can lead to instabilities in the system behavior.
In order to avoid these disadvantages bearings with an elastic air film support, called Gas Foil Bearings (GFB) were developed. The elastic deformation under the impact of the pressure field leads to an optimized gap geometry and increases the bearable load capacity. Furthermore, friction processes during dynamic deformation generate additional, external damping with positive effects on system stability and the rotor vibration level, ref. Heshmat et al [1].
Dellacorte et al [2] made a comparison between bearings with different realizations of the deformable bearing housings up to 1998. The most appreciable solutions were the Leaf (LFB) and the bump-type Bearings (BFB). While Leaf type bearings use the bending stiffness of thin metal sheets, the bump-type bearings make use of a corrugated metal foil. Dellacorte et al. [2] have shown that the steady progression leads to more than four times higher load capacities. These results indicate the high influence of the structure properties for possible operating ranges.
San Andres et al [3] investigated concepts based on a metal mesh as a replacement for the most frequently used bump foils. Metal Mesh Foil Bearings (MMFB) have the advantage of continuous distributed stiffness and damping properties in circumferencial and axial direction. An experimental performance analysis of a BFB and a MMFB with similar size performed by San Andres et al.[4] in 2012 revealed better damping characteristics for the metal mesh type. The determined loss factor as indicator for the external mechanical damping of the MMFB was two times higher than the loss factor of the contemplated BFB. In 2003 Lee et al [5] tried to improve the performance of a common BFB of the first generation by integrating a viscoelastic material between top and bump foil. The Viscoelastic Foil Bearing (VEFB) had superior damping characteristics. Especially near the first bending critical speed and in the range beyond, the magnitude of the rotor amplitudes could be intensively reduced.

Sim and Park [6] executed measurements on an electrical drive with three different bearing types. First conventional BFBs, as second Gas Polymer Bearings (GPB) with a polymer layer instead of the bump foil and as third a hybrid version like Lee et al [5] investigated were used for the rotor support. The results of the experiment are similar to these from Lee. The integration of the polymer layer had positive effects for the dynamic of the driven rotor. The greatest loss factors could be determined for the GPB. It is obvious that viscoelastic materials, especially polymers, offer other benefits, for example a simple manufacturing and the possibility to set material characteristics specifically.

Despite the higher performance of improved structures it is still complicated to conceptualize a system with GFBs. Numerical simulations and measurements have to be conducted. Today, focus in research on GFBs is to build high efficient numerical models to simulate the rotordynamic behavior in order to increase the speed of development processes and reduce its costs. For GPBs only experimental studies are available. Several models for simulations with bump-type-bearings in frequency and time domain were developed up until today. However, numerical models for GPBs do not exist yet. The objective of the present work is to implement a model for transient simulations of a rotor supported by GPBs and to give a description of the frequency domain based parametrization method.

2 Theory

The description of the nonlinear behavior of polymer materials is an important part of research. The dynamic characteristics generally depend on the deformation magnitude and its velocity. Furthermore, the material temperature has a high impact on the polymer properties. With respect to the dominating radial load, which is initialized by the pressure field, all crosswise deformations of the polymer layer will be neglected. Commonly used characterization methods for one-dimensional models consider the material response on harmonic excitation. Based on this, frequency-dependent stiffness and damping coefficients can be determined. Figure (1) illustrates coefficients for a perfluoro-caoutchouc (FFKM), which are based on a master curve by Bormann [7].

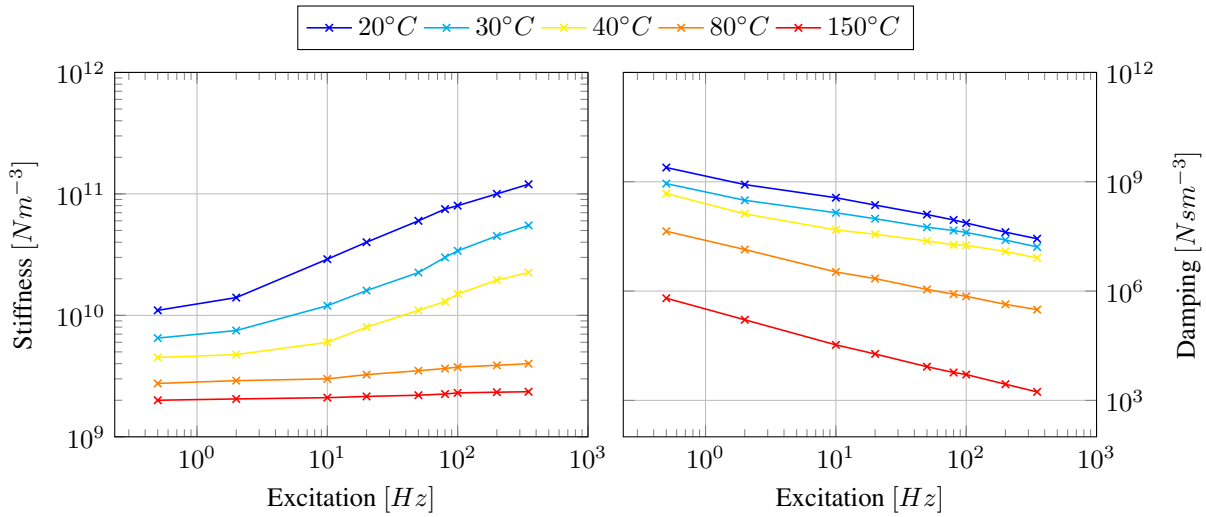

Figure 1: Frequency-dependent stiffness and damping coefficients of a perfluoro-caoutchouc based on a measurement published by Bormann [7]: (left) stiffness coefficients , (right) damping coefficients

The following statements apply in general for polymer materials:

- The stiffness coefficients are increasing with the frequency.
- The damping coefficients are decreasing with the frequency.
- An increase in temperature reduces the stiffness and damping performance.
- For a constant frequency, a higher deformation magnitude results in lower stiffness and higher damping coefficients.

Model Pre-Limitations

The following structure model is an early and simple implementation for the viscoelastic behavior of polymer structures. It considers the frequency dependence of the stiffness and damping coefficients, under the assumption of one-directional displacements without element couplings. Because the model is isothermal, new sets of parameters have to be generated for different temperatures. Due to the small ratio between deformation and layer thickness the dependence of the deformation magnitude is neglected.

3 Structure Model

In order to describe the nonlinear behavior of polymers under dynamic loads, discrete rheological elements are commonly used. These complex elements consist of linear basic elements, like the Hookean (HE) and the Newton element (NE). While the HE corresponds to a linear stiffness the NE represents a linear damper. A nonlinear material behaviour can be modeled by creating networks of these basic elements. A high number of complex networks is available for effects like crawling and relaxation. Based on the generalized Kelvin-Voigt model (GKV) and the generalized Maxwell model (GM) depicted in Figure (2), it is possible to create the behavior of any complex network of HE's and NE's.

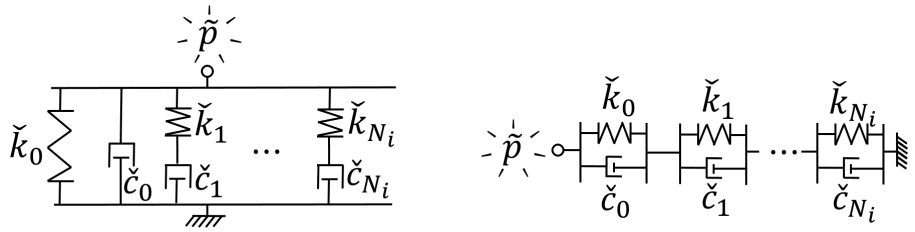

Figure 2: Complex rheological elements with inner parameters for the discrete springs and dampers under the load of a pressure field: (left) Generalized Maxwell Model, (right) Generalized Kelvin-Voigt Model

3.1 Parametrization - Frequency Domain

In order to approximate the frequency dependence for the stiffness and damping coefficients a complex stiffness (with respect to the Complex Shear Module, ref. Popov [8]), can be defined,

$$K^*(\omega) = K^{'}(\omega) + jK^{''}(\omega) \tag{1}$$

where the stiffness and damping coefficient for a specific frequency can be calculated from the real and imaginary part.

$$\tilde{k}(\omega) = \mathrm{Re}\{K^*(\omega)\} \quad , \quad \tilde{c}(\omega) = \mathrm{Im}\{K^*(\omega)\}/\omega \tag{2}$$

With the complex stiffness of the HE and the NE,

$$K^*_{HE} = \check{k} \quad , \quad K^*_{NE} = j\omega\check{c} \tag{3}$$

where $\check{k} = kh_0/p_a$ and $\check{c} = ch_0\Omega/p_a$ are the discrete normalized stiffness and damping values of the basic elements, p_a is the ambient pressure and h_0 is the nominal gap. For the GM and GKV network

$$K^*_{GM}(\omega) = \left[\check{k}_0 + \sum_{i=1}^{N_{re}} \frac{\check{k}_i\check{c}_i^2\omega^2}{\check{k}_i^2 + \check{c}_i^2\omega^2}\right] + j\left[\check{c}_0\omega + \sum_{i=1}^{N_{re}} \frac{\check{k}_i^2\check{c}_i\omega}{\check{k}_i^2 + \check{c}_i^2\omega^2}\right] \tag{4}$$

and

$$K^*_{GKV}(\omega) = \left(\sum_{i=0}^{N_{re}} \frac{1}{\check{k}_i + j\omega\check{c}_i} \right)^{-1} \tag{5}$$

can be obtained. Thus, the given Eqs. (4) and (5) in combination with Eq. (2) enable a comparison between model and measured data. For an initial set of $2N_{re}$ inner parameters $\check{k}_i$ and $\check{c}_i$ with $i = 0, ..., N_{re}$ the local mismatch for each frequency can be determined. It is reasonable to avoid a different weighting for the measured stiffness $\bar{k}$ and damping $\bar{c}$ in the parametrization process. The local difference at ω_k has to be normalized by the measured values $\bar{k}_k$ or $\bar{c}_k$. A high global accordance can be achieved by adding up the local relative errors. To enable a comparison of global errors from measured data sets with different grid sizes the global error is divided by the number of frequency grid points K. The resulting, nonlinear minimization problem is defined in Equation (6).

$$Err = \frac{1}{K} \left[\sum_{k=1}^{K} \left(\tilde{k}_k - \bar{k}_k \right) \frac{1}{\bar{k}_k} + \sum_{k=1}^{K} \left(\tilde{c}_k - \bar{c}_k \right) \frac{1}{\bar{c}_k} \right] \Longrightarrow min \tag{6}$$

In the $2n$-dimensional parameter space a high number of local minimums are located, therefore gradient based minimization methods are not suitable. As solver for the problem, metaheuristical methods like genetic algorithms (GA) or particle swarm optimizer are to prefer.

3.2 Time Domain

In contrast to the frequency domain model, with only one external degree of freedom (DOF), the time domain model needs several inner DOFs. In Figure (3) the extension of the GM and GKV is depicted. For each DOF

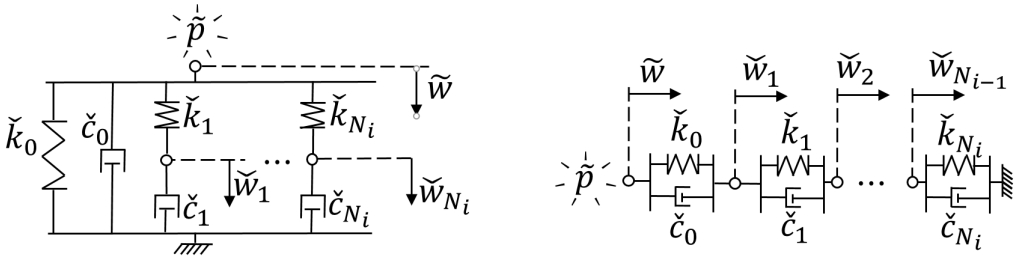

Figure 3: Complex rheological elements with inner parameters for the discrete springs and dampers and inner degrees of freedom, under the load of a pressure field: (left) Generalized Maxwell Model, (right) Generalized Kelvin-Voigt Model

an equilibrium in forces leads to an equation of motion. The Equations (7) up to (9) build a system of ordinary differential equations (ODE) for the GM, which can be solved by common ODE solvers.

$$\tilde{p} = \check{k}_0\tilde{w} + \check{k}_1(\tilde{w} - \breve{w}_1) + \ldots + \check{k}_i(\tilde{w} - \breve{w}_i) + \check{c}_0\dot{\tilde{w}} \tag{7}$$

$$0 = \check{k}_1(\breve{w}_1 - \tilde{w}) + \check{c}_1\dot{\breve{w}}_1 \tag{8}$$

$$\vdots$$

$$0 = \check{k}_n(\breve{w}_n - \tilde{w}) + \check{c}_n\dot{\breve{w}}_n \tag{9}$$

The same procedure for the GKV results in the system of the Equations (10) up to (13).

$$\tilde{p} = \check{k}_0(\tilde{w} - \check{w}_1) + \check{c}_0(\dot{\tilde{w}} - \dot{\check{w}}_1) \tag{10}$$
$$0 = \check{k}_1(\check{w}_1 - \check{w}_2) + \check{c}_1(\dot{\check{w}}_1 - \dot{\check{w}}_2) - \check{k}_0(\tilde{w} - \check{w}_1) - \check{c}_0(\dot{\tilde{w}} - \dot{\check{w}}_1) \tag{11}$$
$$\vdots$$
$$0 = \check{k}_{n-1}(\check{w}_{n-1} - \check{w}_n) + \check{c}_{n-1}(\dot{\check{w}}_{n-1} - \dot{\check{w}}_n) - \check{k}_{n-2}(\check{w}_{n-2} - \check{w}_{n-1}) - \check{c}_{n-2}(\dot{\check{w}}_{n-2} - \dot{\check{w}}_{n-1}) \tag{12}$$
$$0 = \check{k}_n\check{w}_n + \check{c}_n\dot{\check{w}}_n - \check{k}_{n-1}(\check{w}_{n-1} - \check{w}_n) - \check{c}_{n-1}(\dot{\check{w}}_{n-1} - \dot{\check{w}}_n) \tag{13}$$

For both elements the ODE system has the form of Equation (14), with $\mathbf{K}^{(e)}$ and $\mathbf{C}^{(e)}$ as resulting stiffness and damping matrices. The vector $\mathbf{w}$ contains the displacement of the external DOF, which has an impact on the height of the air film. The other DOFs are the inner ones, which do not interact with the fluid film or the rotor. The load vector $\mathbf{f}$ contains the external load initiated by the pressure field.

$$\mathbf{f}^{(e)} = \mathbf{C}^{(e)}\dot{\mathbf{w}}^{(e)} + \mathbf{K}^{(e)}\mathbf{w}^{(e)} \tag{14}$$

4 Transient Model

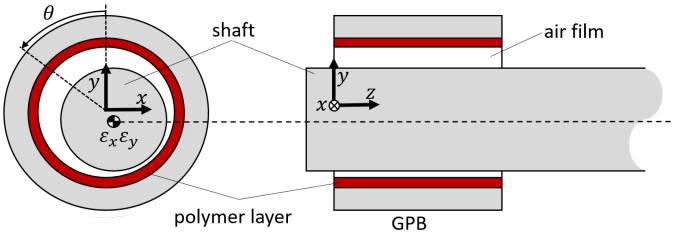

Figure 4: Schematic model of a rotor supported by GPBs

In Figure (4) a rotor supported by GPBs is schematically illustrated. Under the assumption of symmetry, only one bearing and half of the shaft have to be considered. The following model is based on the work of Bonello and Pham [9], who introduced a state variable ψ that allows a simultaneous time integration of the whole rotor-bearing-system. As a model for the fluid film a dimensionless form of the Reynolds Equation (15) is used. The definitions for ψ and the normalized pressure $\tilde{p}$, gap height $\tilde{h}$, time τ and the axial coordinate Z are presented in Equation (16).

$$\frac{\partial\psi}{\partial\tau} = \frac{1}{\Lambda}\left\{\frac{\partial}{\partial\Theta}\left[\psi\left(\tilde{h}\frac{\partial\psi}{\partial\Theta} - \psi\frac{\partial\tilde{h}}{\partial\Theta}\right)\right] + \frac{\partial}{\partial Z}\left[\psi\left(\tilde{h}\frac{\partial\psi}{\partial Z} - \psi\frac{\partial\tilde{h}}{\partial Z}\right)\right]\right\} - \frac{\partial\psi}{\partial\Theta} \tag{15}$$

$$\psi = \tilde{p}\tilde{h} \quad , \quad \tilde{p} = \frac{p}{p_a} \quad , \quad \tilde{h} = \frac{h}{h_0} \quad , \quad \tau = \frac{\Omega}{2}t \quad , \quad Z = \frac{L}{R} \tag{16}$$

To create a system of ODEs from the partial differential equation (15), finite difference formulas were used to approximate the derivatives. The discretization of Equation (15), with N_Θ and N_Z grid points in circumferential and axial direction, can be written in a vectorized form, see Equation (17). It has to be mentioned that all vectors have to be multiplied elementwise.

$$\frac{d\boldsymbol{\psi}}{d\tau} = \frac{1}{\Lambda}\left(\tilde{\boldsymbol{h}}\left(\frac{\partial\boldsymbol{\psi}}{\partial\Theta}\frac{\partial\boldsymbol{\psi}}{\partial\Theta} + \frac{\partial\boldsymbol{\psi}}{\partial Z}\frac{\partial\boldsymbol{\psi}}{\partial Z}\right) + \tilde{\boldsymbol{h}}\boldsymbol{\psi}\left(\frac{\partial^2\boldsymbol{\psi}}{\partial\Theta^2} + \frac{\partial^2\boldsymbol{\psi}}{\partial Z^2}\right) - \boldsymbol{\psi}\left(\frac{\partial\tilde{\boldsymbol{h}}}{\partial\Theta}\frac{\partial\boldsymbol{\psi}}{\partial\Theta} + \frac{\partial\tilde{\boldsymbol{h}}}{\partial Z}\frac{\partial\boldsymbol{\psi}}{\partial Z}\right) - \boldsymbol{\psi}^2\left(\frac{\partial^2\tilde{\boldsymbol{h}}}{\partial\Theta^2} + \frac{\partial^2\tilde{\boldsymbol{h}}}{\partial Z^2}\right)\right) - \frac{\partial\boldsymbol{\psi}}{\partial\Theta} \tag{17}$$

The differential equation for the rotor is defined in Equation (18), where the vector $\boldsymbol{\varepsilon} = \{\varepsilon_x, \varepsilon_y\}^T$ contains the displacement of the shaft center normalized by the nominal gap h_0. The tilting DOFs are neglected under the assumption of a symmetric system.

$$\frac{d^2}{d\tau^2}\boldsymbol{\varepsilon} = \frac{4}{m_r h_0 \Omega^2}(\mathbf{f}_f + \mathbf{f}_u + \mathbf{f}_p) \tag{18}$$

The motion of the rotor depends on the three force components on the right hand side of the system. The vector $\mathbf{f}_f$ contains the gravitational force and $\mathbf{f}_u$ gives the effect of the unbalance, see. Equations (19). Both forces are rotor specific ones,

$$\mathbf{f}_f = \{0, m_r g\}^T \quad , \quad \mathbf{f}_u = \hat{F}_u\{\sin(2\tau), \cos(2\tau)\}^T \tag{19}$$

whereas the vector $\mathbf{f}_p$ contains the gas forces induced by the pressure field, see Equation (20).

$$\mathbf{f}_p = -p_a R^2 \int_0^{2\pi} \int_0^{R/L} \left\{ \frac{\psi}{\tilde{h}} - 1 \right\} \begin{bmatrix} \cos(\Theta) \\ \sin(\Theta) \end{bmatrix} dZ d\Theta \tag{20}$$

The second order equation (18) has to be transformed into state space to enable a later use of standardized ODE solvers, ref. Equation (21).

$$\frac{\partial}{\partial \tau}\begin{pmatrix} \boldsymbol{\varepsilon} \\ \dot{\boldsymbol{\varepsilon}} \end{pmatrix} = \begin{pmatrix} \dot{\boldsymbol{\varepsilon}} \\ \frac{4}{m_r h_0 \Omega^2}(\mathbf{f}_f + \mathbf{f}_u + \mathbf{f}_p) \end{pmatrix} \tag{21}$$

As approximation for the structure behavior, a Nonlinear Viscoelastic Foundation Model (NVEFM) is realized by a single GM or GKV element for each angular mesh position. At a discrete node the load for each structure element corresponds to the mean value of the pressure in axial direction. The ODE system of the structure given in Equation (22) is an assembly of the element formulation in analogy to Equation (14),

$$\mathbf{f}_S = \mathbf{C}_S \dot{\mathbf{w}}_\mathbf{S} + \mathbf{K}_S \mathbf{w}_S \tag{22}$$

with

$$\mathbf{f}_S = \{f^e_{1,1}, f^e_{1,2}, \ldots, f^e_{1,N_Z}, \ldots, f^e_{N_\Theta,1}, \ldots, f^e_{N_\Theta,N_Z}\}^T, \tag{23}$$

$$\mathbf{w}_S = \{w^e_{1,1}, w^e_{1,2}, \ldots, w^e_{1,N_Z}, \ldots, w^e_{N_\Theta,1}, \ldots, w^e_{N_\Theta,N_Z}\}^T, \tag{24}$$

$$diag(\mathbf{C}_S) = \{\mathbf{C}^e_{1,1}, \mathbf{C}^e_{1,2}, \ldots, \mathbf{C}^e_{1,N_Z}, \ldots, \mathbf{C}^e_{N_\Theta,1}, \ldots, \mathbf{C}^e_{N_\Theta,N_Z}\}, \tag{25}$$

$$diag(\mathbf{K}_S) = \{\mathbf{K}^e_{1,1}, \mathbf{K}^e_{1,2}, \ldots, \mathbf{K}^e_{1,N_Z}, \ldots, \mathbf{K}^e_{N_\Theta,1}, \ldots, \mathbf{K}^e_{N_\Theta,N_Z}\}. \tag{26}$$

In order to transform the system to the same form as Equation (17) and (21), the Equation (22) has to be rewritten as follows:

$$\dot{\mathbf{w}}_S = \mathbf{C}_S^{-1}(\mathbf{f}_S - \mathbf{K}_S \mathbf{w}_S). \tag{27}$$

The normalized height of the gap at each discrete point of the fluid film grid can be calculated with Equation (28). It defines the gap geometry for the fluid film and depends on the rotor displacements and the structure deformation. The simultaneous coupling of the system is defined by Equation (28) in combination with Equation (20) for all $a = 1 \ldots N_\Theta$ and $b = 1 \ldots N_Z$.

$$\tilde{h}_{a,b} = 1 - \varepsilon_x \cos(\Theta_a) - \varepsilon_y \sin(\Theta_a) + \tilde{w}_{a,b} \tag{28}$$

Boundary Conditions

The objective with subsequent bearing prototypes is to manufacture the bearings by an injection molding process with a closed loop top foil. The absence of the fixture point is considered by using a continuous, circular condition for the mesh ends in circumferential direction, ref. Equations (29) and (30).

$$\psi_{N_\Theta+1,b} = \psi_{1,b} \qquad b = 1 \dots N_Z \tag{29}$$

$$\tilde{h}_{N_\Theta+1,b} = \tilde{h}_{1,b} \qquad b = 1 \dots N_Z \tag{30}$$

At the bearing edges, constant ambient pressure is assumed, for that reason the edges are removed from the fluid film and structure mesh. Nevertheless the assumption of the constant ambient pressure has to be considered for the derivatives, for all $a = 1 \dots N_\Theta$ the Equation (31) is used in the finite difference formulas.

$$\psi_{a,N_{Z+(1)}} = \tilde{h}_{a,N_{Z+(1)}} \quad , \quad \psi_{a,1-(1)} = \tilde{h}_{a,1-(1)} \tag{31}$$

The gap function at the bearing edges, see Equations (32) and (33), depends on the deformation of the structure. By the assumption of ambient pressure, theoretically there is no deformations at the edges. However, for the purpose of considering the axial bending stiffness of the top foil, a constant deformation in axial direction is implemented.

$$\tilde{h}_{a,N_{Z+(1)}} = 1 - \varepsilon_x \cos(\Theta) - \varepsilon_y \sin(\Theta) + \tilde{w}_{a,N_{Z+(1)}} \tag{32}$$

$$\tilde{h}_{a,1-(1)} = 1 - \varepsilon_x \cos(\Theta) - \varepsilon_y \sin(\Theta) + \tilde{w}_{a,1-(1)} \tag{33}$$

5 Numerical results

The results presented are based on the data set of the FFKM at a temperature of $T = 20°C$ and were calculated for a material thickness of $t_L = 2mm$. As solver for the minimization problem, a genetic algorithm was used. Figure (5) shows the resulting coefficients for a GM and a GKV model with a number of $2N_{de} = 14$ discrete springs and dampers. In general the increasing character of the stiffness and the decreasing behavior of the damping are well represented by both models.

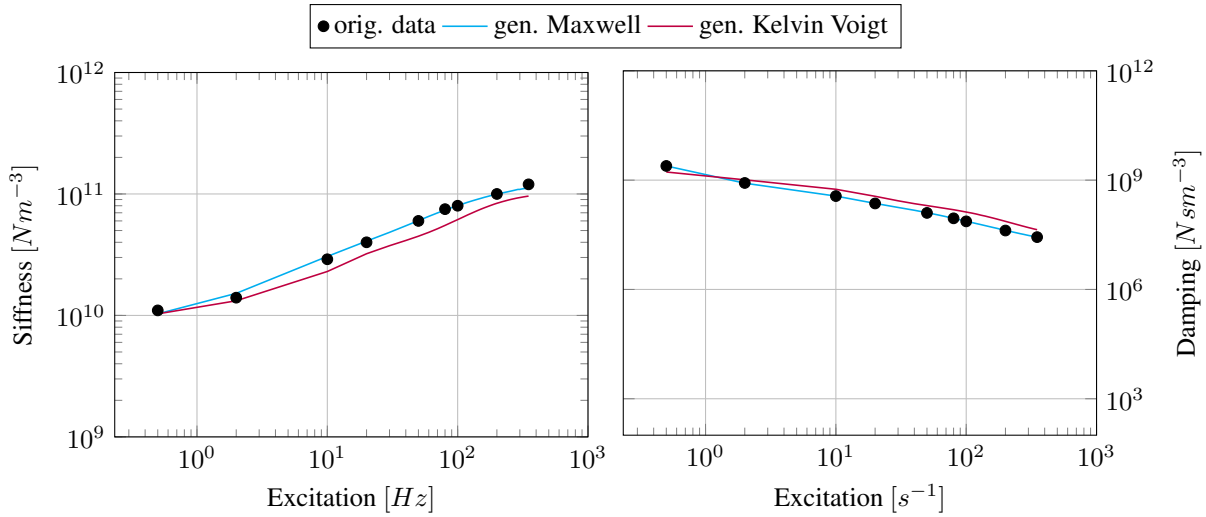

Figure 5: Frequency dependent stiffness and damping coefficients generated by the GM and the GKV models in comparison to the original measured coefficients: (left) stiffness, (right) damping

In Figure (6) the local, relative discrepancy of the coefficients from the original data is depicted. For each excitation frequency the local error for the GM is less than 10%. The parameter set for the GKV has a higher discrepancy to the measured data. The local relative errors are only in the same decade of the measured data. The

approximation quality has to be improved in future development. For both models it is theoretically possible to approximate the data set in the same quality, but due to the series build character of the GKV it is more difficult to find suitable parameters. Inside of the GM model each pair, consisting of a discrete spring and damper, has a specific character in the frequency domain without influence on other pairs. Furthermore, it is possible to control the activation frequency for a discrete spring by its damping parameter. In contrast every change of a parameter inside of the GKV can in- or decrease the effect of other pairs.
As mentioned before, the mountainous landscape character of the minimization problem in Equation (6) leads to parameter sets, that represent local minimums. Regarding to the stochastically generated initial population, it is unlikely to regenerate the exact same solution twice. Nevertheless, the dynamic behavior of two sets with nearly the same global error level is very similar. A higher number of discrete elements can lead to a better concurrence between model and measured data, but also increases the numerical effort in the time domain. Furthermore it becomes more difficult to define the parameter ranges for the sampler and the optimizer. On the experimental side, the measurement of more data points in frequency domain even has a positive effect.

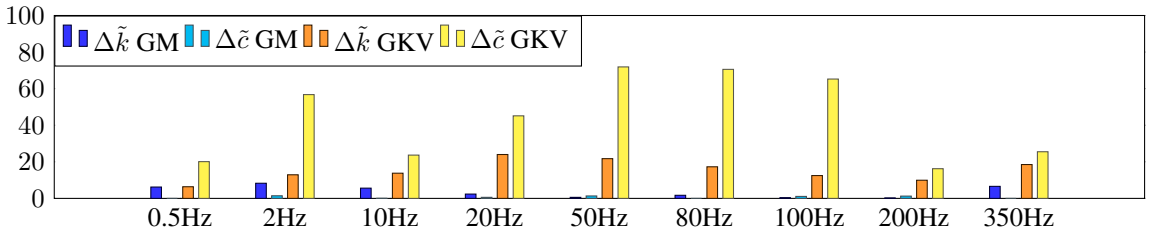

Figure 6: Overview of the local model discrepancy, for the generalized Maxwell Model and the Generalized Kelvin-Voigt Model, relative to the coefficients of the measured coefficients from literature

The transient model pertains to the properties listed in Table (2), while the generated parameter sets for the GM and the GKV are listed in Table (1). The mesh size for the fluid film is $N_\Theta \times N_Z$ with $N_\Theta = 72$ and $N_Z = 24$. The structure contains N_Θ generalized elements. The resulting trajectories describe the motion of the rotor falling from the center position at a constant rotational speed. As solver for the ODE system an explicit 3rd-order Runge-Kutta-Method with embedded step control was used.

	GM		GKV	
i	$\check{k}_i$	$\check{c}_i$	$\check{k}_i$	$\check{c}_i$
0	1.362E+09	1.605E+07	2.950e+010	1.612e+010
1	4.150E+10	1.110E+08	1.182e+011	2.380e+007
2	5.767E+09	2.988E+09	2.505e+010	1.690e+009
3	1.735E+10	4.522E+08	1.062e+009	6.466e+010
4	6.400E+09	3.303E+09	4.816e+010	2.623e+010
5	1.125E+10	1.135E+08	8.855e+010	5.186e+008
6	3.946E+10	3.120E+07	7.500e+010	3.527e+010

Table 1: Damping and stiffness parameters for the generalized Maxwell-Model

RBS parameter			
half of rotor mass	m_r	5.0	kg
bearing radius	R	20	mm
bearing length	L	40	mm
nominal clearance	h_0	50	μm
air viscosity	μ	19.5	N/mm^2
ambient pressure	p_a	0.1	MPa
FFKM thickness	t_L	2	mm

Table 2: Damping and stiffness parameter for the generalized Maxwell-Model

Figure (7) illustrates the trajectories for the RBS without unbalance for different rotational speeds. Despite the difference in the approximation quality, both models show a similar behaviour for each case. In the simulation for

$12krpm$ on the left side, the center of the rotor moves quickly to its equilibrium position. Shortly before the spiral movement of the rotor ends, a creep effect can be detected. These effects are typical for polymers. Regarding the model, this effect is caused by the gradually decreasing influence of the discrete dampers. Thus, for the GM the static equilibrium position of the rotor center is the same, as for a simulation with only the parameter $\check{k}_0$. The simulations with $18krpm$ and $24krpm$ show, that the magnitude of the shaft motion increases with the rotor

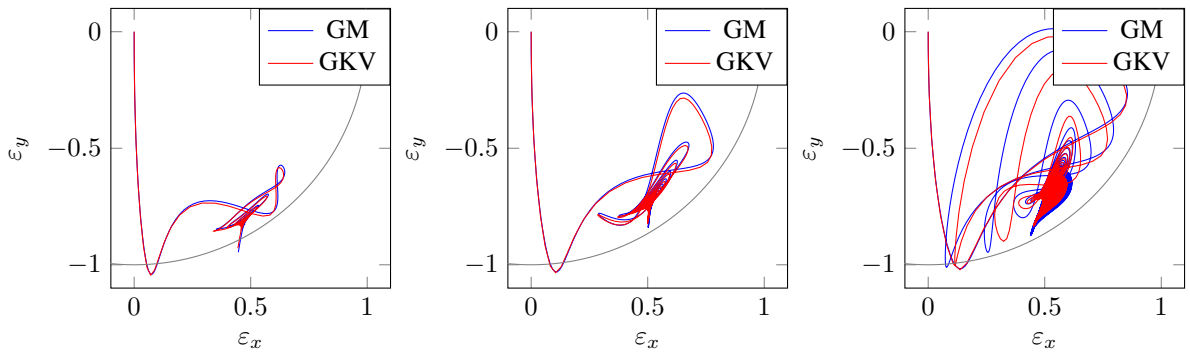

Figure 7: Trajectories of the shaft center under different rotational speeds: (left) at 12000rpm, (middle) at 18000rpm, (right) at 24000rpm

speed. In case of $24krpm$ the center does not reach an equilibrium, because of sub harmonic vibrations. In Figure (8) the normalized shaft displacement ε_x in horizontal direction over time is illustrated for $18krpm$, $24krpm$ and $25krpm$. The initial vibration for $18krpm$ disappears quickly, whereas the vibration for $24krpm$ rises. As shown in the lower figure, for higher speeds the motion of the shaft becomes dominated by a subharmonic vibration, after a short period of time.

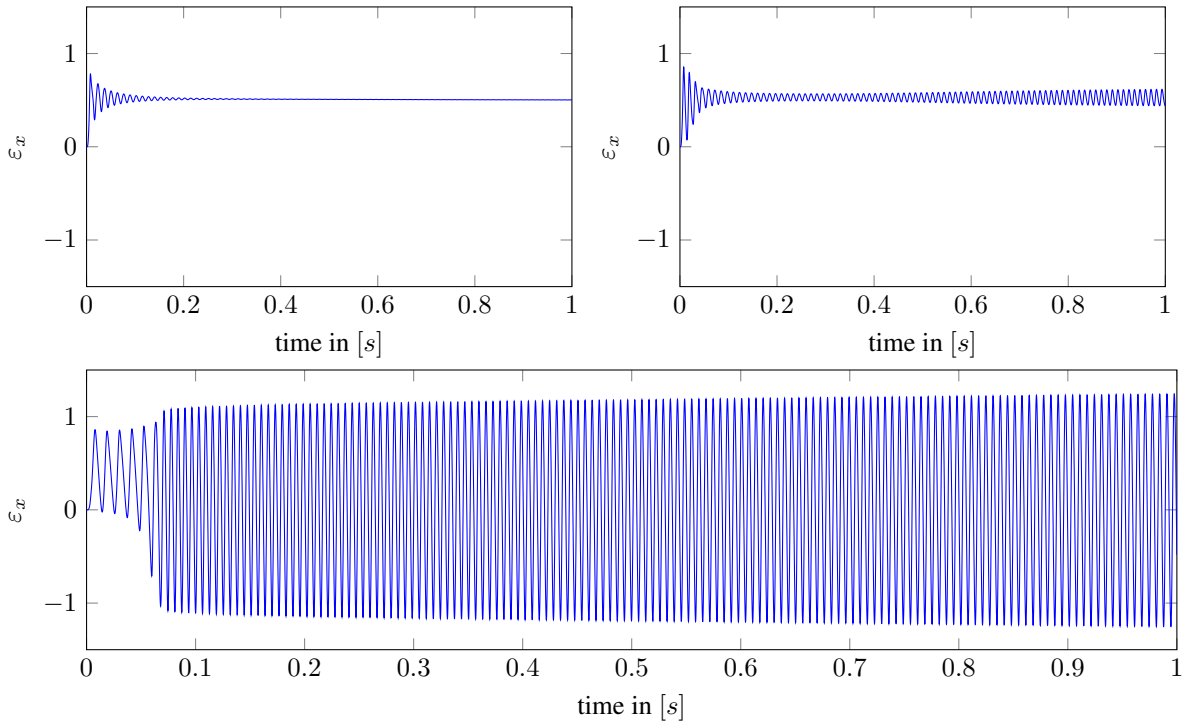

Figure 8: Time signals for the motion component in horizontal direction: (upper left) at 18000rpm, (upper right) at 24000rpm, (bottom) at 25000rpm

6 Conclusion

This paper's overall contribution has been the implementation of a structure model for analysis of rotors supported by Gas Polymer Bearings in the time domain. The developed Nonlinear Viscoelastic Foundation Model uses generalized rheological elements to include the frequency dependent behaviour of polymers. Furthermore, the description of a procedure to generate suitable parameter sets for the structure model was subject of this paper. Due to the neglected temperature and amplitude dependencies, the presented NVEFM has to be seen as an early basic model, which has to be expanded in future. For the enhancements it is essential to perform an experimental material study with respect to the required information density.
The next phase of research includes the set up of a test rig to build a data basis, to validate the material models on the measured data and to develop GPB-prototypes for rotordynamic analysis.

REFERENCES

[1] Heshmat, H., 1994. "Advancements in the performance of aerodynamic foil journal bearings: High speed and load capability". *Journal of Tribology,* **116**(2), S. 287.

[2] Dellacorte, C., and Valco, M. J., 2000. "Load capacity estimation of foil air journal bearings for oil-free turbomachinery applications". *Tribology Transactions,* **43**(4), jan, S. 795–801.

[3] San Andrés, L., Chirathadam, T. A., and Kim, T.-H., 2010. "Measurement of structural stiffness and damping coefficients in a metal mesh foil bearing". *Journal of Engineering for Gas Turbines and Power,* **132**(3), S. 032503.

[4] San Andrés, L., and Chirathadam, T. A., 2012. "A metal mesh foil bearing and a bump-type foil bearing: Comparison of performance for two similar size gas bearings". *Journal of Engineering for Gas Turbines and Power,* **134**(10), S. 102501.

[5] Lee, Y.-B., Kim, T.-H., Kim, C.-H., Lee, N.-S., and Choi, D.-H., 2004. "Dynamic characteristics of a flexible rotor system supported by a viscoelastic foil bearing (VEFB)". *Tribology International,* **37**(9), sep, S. 679–687.

[6] Sim, K., and Park, J., 2017. "Performance measurements of gas bearings with high damping structures of polymer and bump foil via electric motor driving tests and one degree-of-freedom shaker dynamic loading tests". *Journal of Engineering for Gas Turbines and Power,* **139**(9), apr, S. 092504.

[7] Bormann, A., 2005. *Elastomerringe zur Schwingungsberuhigung in der Rotordynamik: Theorie, Messungen und optimierte Auslegung*. Fortschritt-Berichte VDI: Reihe 11, Schwingungstechnik. VDI-Verlag.

[8] Popov, V. L., 2017. *Contact Mechanics and Friction*. Springer Berlin Heidelberg.

[9] Bonello, P., and Pham, H., 2014. "The efficient computation of the nonlinear dynamic response of a foil–air bearing rotor system". *Journal of Sound and Vibration,* **333**(15), jul, S. 3459–3478.

Nomenclature

p	pressure
k, K	stiffness
c	damping coefficient
w	structure deformation
h	gap height
m_r	rotor mass
L	axial bearing length
R	bearing radius
ε	norm. rotor displacement
Λ	$= 6\mu\Omega/p_a(R/h_0)^2$
μ	air viscosity
ω	excitation frequency
Ω	rotational speed
ψ	ph couple value

$\mathbf{K}$	stiffness matrix
$\mathbf{C}$	damping matrix
$\mathbf{f}$	force vector
$\boldsymbol{\varepsilon}$	rotor displacement vector
$\tilde{(\cdot)}$	normalized external value
$\check{(\cdot)}$	normalized inner value
$(\cdot)^*$	complex value
$\bar{(\cdot)}$	measured normalized value
$\dot{(\cdot)}$	time derivative
Z, Θ	polar coordinates
x, y	cartesian coordinates